

PAPER

## An empirical potential for simulating vacancy clusters in tungsten

To cite this article: D R Mason *et al* 2017 *J. Phys.: Condens. Matter* **29** 505501

View the [article online](#) for updates and enhancements.

### You may also like

- [Potential Dependence of Intergranular Corrosion Propagation in Sensitized Al-Mg Alloys](#)  
Mary Lyn C. Lim, David W. Ellis, Stewart C. Hahn et al.
- [Red Blood Cells Morphology Depending on Potential of Optically Transparent Electrode](#)  
Mogely Sh. Khubutiya, Anatoly K. Evseev, Mojtaba Mirzaeian et al.
- [\(Invited\) Large Mobility Modulation Due to Discrete Impurities in Nanowires](#)  
Nobuyuki Sano

# An empirical potential for simulating vacancy clusters in tungsten

D R Mason<sup>1</sup> , D Nguyen-Manh<sup>1</sup> and C S Becquart<sup>2</sup>

<sup>1</sup> CCFE, Culham Centre for Fusion Energy, Abingdon, Oxfordshire OX14 3DB, United Kingdom

<sup>2</sup> Univ. Lille, CNRS, INRA, ENSCL, UMR 8207, UMET, Unité Matériaux et Transformations, F 59 000, Lille, France

E-mail: [daniel.mason@ukaea.uk](mailto:daniel.mason@ukaea.uk)

Received 21 September 2017, revised 26 October 2017

Accepted for publication 1 November 2017

Published 27 November 2017



## Abstract

We present an empirical interatomic potential for tungsten, particularly well suited for simulations of vacancy-type defects. We compare energies and structures of vacancy clusters generated with the empirical potential with an extensive new database of values computed using density functional theory, and show that the new potential predicts low-energy defect structures and formation energies with high accuracy. A significant difference to other popular embedded-atom empirical potentials for tungsten is the correct prediction of surface energies. Interstitial properties and short-range pairwise behaviour remain similar to the Ackford-Thetford potential on which it is based, making this potential well-suited to simulations of microstructural evolution following irradiation damage cascades. Using atomistic kinetic Monte Carlo simulations, we predict vacancy cluster dissociation in the range 1100–1300 K, the temperature range generally associated with stage IV recovery.

Keywords: empirical potential, vacancy cluster, surface energy, tungsten

(Some figures may appear in colour only in the online journal)

## 1. Introduction

High-purity tungsten has some exceptional physical properties. As well as being a refractory metal with the highest elemental melting point (3690 K), it has the lowest coefficient of thermal expansion, and very high thermal conductivity. Combined with its high resistance to sputtering, and the fact that under fusion neutron irradiation its transmutation products are considered acceptable [1, 2], these qualities have lead to its choice as a material for the ITER divertor [3–5]. However, tungsten is brittle, and its thermomechanical properties become worse on irradiation [6–8], so a key aim of fusion materials research is to understand the atomistic processes of irradiation damage generation, and how the accumulation of such damage acts as an impedance to dislocation motion and hence a reduction in plasticity.

After the initial high-energy generation of defects by radiation cascade damage, the underlying processes governing defect cluster interactions will be due to by small adjustments of chemical bonds for atoms in non-perfect-crystal arrangements. Density functional theory (DFT), with appropriate

choice of functional used, is the standard workhorse for calculating these changes in electronic bonding [9]. But the microstructural evolution driven by the competition between these subtle energy differences and configurational entropy emerges in systems of many thousands of atoms, and over timescales of years. Empirical potentials are therefore still routinely required for simulations of collective dynamic behaviours, and will continue to be so as computing power brings into range ever more ambitious molecular dynamics and kinetic Monte Carlo simulations.

Work on the new empirical parameterization presented here was motivated by conflicting experimental and theoretical observations on vacancy-type dislocation loops generated by self-ion-irradiation of ultra-high-purity tungsten foil. In 2008, Gilbert *et al* [10] computed the relative stability of nanoscale vacancy-type defects in tungsten, and concluded that voids would be the most stable configuration of vacancies. They also showed, using a potential by Derlet *et al* [11] that small vacancy type dislocation loops (diameter <3.5 nm) were unstable with respect to transformation to void plates. Sand *et al*, using the potential of Derlet *et al* [11], stiffened at short

range for cascade simulations by Björkas *et al* [12], showed that molecular dynamics simulations of radiation damage cascades in bulk tungsten [13], and in foil [14] produced rather diffuse vacancy-rich regions, and interstitial-type dislocation loops. This result was confirmed by Setyawan *et al* [15] using the Juslin and Wirth potential [16]. By contrast, experiments by Jäger and Wilkens [17] and subsequently *in situ* TEM studies of self-ion-irradiation of ultra-high-purity tungsten foils by Yi *et al* [14, 18, 19] have shown that stable nanoscale vacancy loops are indeed generated in radiation damage cascades; in fact they may be as numerous as interstitial type loops. A further well-established issue for EAM potentials is the stability of the divacancy in tungsten. As discussed in [22], empirical potentials typically make the divacancy binding, whereas DFT calculations indicate a vacancy pair should have little interaction [21], or even repel each other [22].

Comparisons between tungsten empirical potentials have been made previously in the literature [22–26], and this manuscript makes no attempt at a comprehensive review. In section 2 we show that one principal problem with earlier potentials was a low surface energy, and that this may be increased without significantly affecting near-equilibrium properties by adjusting the embedding function. In section 3 we discuss vacancy clusters in pure tungsten in detail, and provide dozens of new *ab initio* calculations which are used as a database to prove our new parameterization. Finally we perform atomistic kinetic Monte Carlo simulations in section 4, which show that the characteristic dissociation temperature for vacancy clusters is in the stage IV recovery range 1100–1300 K, and compare our results to recent experiments by Ferroni *et al* [27].

We present a pure tungsten-tungsten potential, aware that many interesting technological applications of tungsten depend on the properties of alloys or interstitial solutes. We leave it to future work to extend this potential for use with vacancy-rhenium [28], vacancy-hydrogen [29–31] and vacancy-helium [31, 32] interactions.

## 2. A modified Finnis–Sinclair potential for tungsten

The Finnis–Sinclair (FS) family [33] of embedded-atom empirical potentials are a popular starting point for atomistic simulation. Their longevity is due to their transferability, which in turn is thanks to their simple form- analytic and (largely) smooth in its derivatives. They are also somewhat underfitted, reproducing lattice parameters and elastic constants, rather than intricate defect properties.

In this development of the tungsten potential, we introduce smoothly-varying, physically-motivated corrections to the original FS form. Each correction improves a desired physical property almost independently, so while many additional parameters are presented, their fitting was not onerous, nor are the physical properties presented in section 3 especially sensitive to their values.

For an embedded-atom potential, the energy of atom  $i$  is written as

$$E_i = \frac{1}{2} \sum_{j \neq i} V(r_{ij}) + F[\rho_i], \quad (1)$$

where  $V(r)$  is a pairwise potential energy, repulsive at short range, and  $F[\rho]$  an embedding function for an atom in a region of electron density  $\rho$ , given by

$$\rho_i = \sum_{j \neq i} \phi(r_{ij}). \quad (2)$$

We will retain this form, making modifications in the form of piecewise polynomial additions to  $V(r)$  and  $F[\rho]$ . We will not add new terms to equation (1). Our justifications for this choice are made below.

### 2.1. Surface energy and void formation energy

A well-known issue with embedded-atom potentials for bcc metals is the underestimation of surface energies [23]. A related issue for tungsten potentials is the overestimation of the vacancy cluster binding energies. The atoms around a vacancy cluster do not significantly relax, so there is little freedom to improve the radial terms  $V(r)$  or  $\phi(r)$ . Atoms in surface- and vacancy- environments are in low-electron-density regions. We can recognise these atoms when the electron density  $\rho_i$  drops significantly below that in the perfect lattice. Therefore we can raise the energy of atoms in surface- and vacancy- environments by increasing (making more positive) the embedding function  $F[\rho]$ .

In the second moment approximation and at zero electronic temperature, we write that the embedding energy is directly proportional to the local electron bandwidth,  $W$ , i.e.  $F[\rho] \sim W[\rho]$ . At electron densities comparable to the perfect lattice, the bandwidth goes as the square root of the density,  $W[\rho] \sim \sqrt{\rho}$ . Where  $\rho$  is low, we want to reduce bonding by reducing the bandwidth, so instead consider an affine form-  $W[\rho] = W_0 + W_1\rho$ . At very low density we must recover  $F[\rho = 0] = 0$ , or the cohesive energy will be changed, so we suggest a polynomial between  $\rho = 0$  and the first intercept between affine and square root forms. We ensure a smooth transition between affine and square root forms at high density with a polynomial interpolation. We therefore have four new parameters to fit; two for the affine form and two for the range of the transition to square-root form. The values of these parameters have been linear-least-squares fitted to the DFT values for vacancy clusters of size 2–5 [21], and the resulting embedding function is illustrated in figure 1. The full parameterization of the embedding function is given in appendix.

### 2.2. Repulsive potential: long range

The long-range part of the Finnis–Sinclair pairwise potential is discontinuous in its second derivative at the cutoff length. This can lead to unexpected behaviour in lattice statics when comparing vibrational free energy between structures where atoms move across this cutoff. This is remedied by smoothly interpolating to zero between second- and third- nearest neighbours with a 7th order polynomial, with continuous first, second and third derivatives at each end.

The regions between equilibrium neighbour separations are important for interstitial formation energies. Rather than

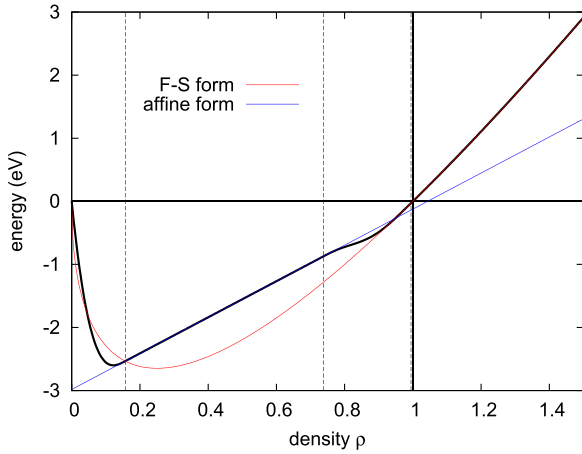


**Figure 1.** The electronic embedding function plotted against electron density for the modified EAM potential. Note that in the gauge used the equilibrium electron density is  $\rho = 1$  and  $F[0] = F[1] = 0$ . The dashed lines mark transitions between sections of the piecewise form, from left to right  $\rho_-, \rho_1, \rho_2$ . These mark the transition from very low density to affine form, and the polynomial switching region from affine to square root form.

attempting a refit of the interstitial properties, which would necessarily have a knock-on effect on dislocation cores too, we chose a maximum range such that the magnitude of the second derivative is minimised in the interpolation region. Therefore while the long-range correction introduces a new cutoff parameter, it is not empirically fitted. Our potential returns similar interstitial and dislocation properties to the Ackland–Thetford parameterization.

### 2.3. Repulsive potential: short range

The short-range part of the Finnis–Sinclair pairwise potential was stiffened by Ackland and Thetford [34] to better describe pairs of atoms in close proximity. It is now conventional for radiation cascade simulations to further stiffen at very-short-range by transitioning smoothly to the universal ZBL pairwise form [35, 36]. We tweak the Ackland–Thetford parameters slightly to better fit DFT data using the method of [37], and transition to ZBL using a polynomial switching function. Between  $r = 2.5$  Å and  $r = 3.25$  Å (covering first and second nearest neighbour separations) there is very little difference between our new parameterization and the Ackland–Thetford form.

## 3. Results

### 3.1. DFT calculations

Density functional theory calculations described in this work were performed using the Vienna *ab initio* simulation package code, with ion-electron interaction implemented using the projector-augmented waves method [38–40]. Exchange and correlation effects were described by the Perdew–Burke–Ernzerhof generalized gradient approximation [41]. A kinetic energy cutoff of 400 eV was used, with  $3 \times 3 \times 3$  k-points. The calculation cell size used was  $5 \times 5 \times 5$  cubic bcc cells (250 atoms) unless otherwise stated.

### 3.2. Point-defect and defect cluster properties

The formation energies and relaxation volumes of the self-interstitials is given in table 1. It should be noted that the cell size used for these calculations is very small, in order to allow the direct comparison with DFT, and there is a significant size effect. At  $5 \times 5 \times 5$  unit cells, the formation energy of the lowest energy interstitial, the  $\langle 111 \rangle_c$  crowdion, falls to 8.99 eV, and is only converged fully to 8.94 eV at  $7 \times 8 \times 9$  unit cells (1008 + 1 atoms).

We present vacancy cluster formation energies and relaxation volumes in table 2. Structures for the vacancy clusters are shown in figure 2. To order vacancy clusters we introduce a single order parameter which indicates the degree of compactness. For a cluster containing  $N$  vacancies in a structure with nearest neighbour separation  $d_0$  ( $= \sqrt{3/4}a_0$  for b.c.c.), we can define an order parameter

$$\chi \equiv \frac{\sum_{i,j>i} \frac{|r_{ij}|^2}{d_0^2}}{\frac{1}{2}N(N-1)}. \quad (3)$$

This takes the minimum value of 1 if all vacancies are nearest neighbours, and is larger for more diffuse structures.

While most bcc metals have a positive binding energy for divacancies, tungsten and (to a lesser extent) molybdenum have little or no interaction between pairs of vacancies in nearest neighbour positions, and indeed vacancy pairs strongly repel each other in next-nearest-neighbour configurations [22, 47]. However, a trend for tungsten empirical potentials is to grossly overestimate the binding energy for vacancy clusters, potentially leading to erroneous conclusions about the readiness to nucleate and grow clusters and voids in a vacancy-rich region. As a single comparable number across potentials we consider the nearest neighbour divacancy (2v1). Our DFT calculations suggest the nearest neighbour divacancy binding energy is very slightly positive at 0.048 eV, in line with previous calculations [21, 22, 29, 30, 47]. There is some considerable debate about the direct experimental estimate of the divacancy binding energy by Park *et al* [48], 0.7 eV, owing to the (necessarily) rather small sample taken in the FIM study. A small concentration of carbon impurities in the experimental sample may also have greatly increased the probability of finding divacancies. We should therefore prefer to rely on the DFT calculation as our reference.

For our comparison, we principally use three potentials from the literature, all of which are commonly used for radiation damage modelling. ‘CEA-4’ is parameterization 4 taken from Marinica *et al* [23]. ‘DND’ is taken from Derlet *et al* [11]. ‘AT’ is taken from Ackland and Thetford [34]. These three EAM-type potentials give strong divacancy binding at 0.518, 0.567 and 0.432 eV respectively. The bond-order potential of Ahlgren *et al* [49] is slightly higher at 0.656 eV Å<sup>-2</sup>, as is the MEAM potential of Zhang *et al* [50] (0.580 eV). Our potential stands alone with a good estimate of the nearest neighbour binding energy of 0.170 eV. We believe our potential is also the only one to have negative binding energies for the second- and third- neighbour divacancies. A summary of vacancy cluster results is given in table 2.

**Table 1.** Self-interstitial properties computed for a relaxed  $4 \times 4 \times 4$  cell ( $128 + 1$  atoms). We consider the SIA dumbbell oriented along  $\langle 111 \rangle$ ,  $\langle 110 \rangle$ , and  $\langle 100 \rangle$  directions (denoted with subscript  $d$ ) and the crowdion oriented along  $\langle 111 \rangle$  (denoted with subscript  $c$ ). Energies in eV, formation volume as fraction of the atomic volume. DFT values from (d) Muzyk *et al* [21], (e) Nguyen-Manh and Dudarev [42] and (f) Nguyen-Manh *et al* [43]. Other empirical potential results computed from analytic forms in (a) Marinica *et al* [23], (b) Derlet *et al* [11], (c) Ackland–Thetford [34].

Configuration	Energy					Formation volume				
	DFT	This work	other EAM			DFT	This work	other EAM		
			(a)	(b)	(c)			(a)	(b)	(c)
$\langle 111 \rangle_d$	10.086 <sup>d</sup> , 9.548 <sup>f</sup>	9.33	10.52	9.46	9.25	1.68 <sup>e</sup>	1.57	1.17	1.33	1.57
$\langle 111 \rangle_c$	9.551 <sup>f</sup>	9.31	10.50	9.46	9.22		1.58	1.10	1.25	1.55
$\langle 110 \rangle_d$	10.545 <sup>d</sup> , 9.844 <sup>f</sup>	9.56	10.75	9.78	9.51		1.62	1.67	1.11	1.54
$\langle 100 \rangle_d$	12.200 <sup>d</sup> , 11.49 <sup>f</sup>	9.74	12.71	11.67	9.77		1.45	1.34	1.03	1.33
tetrahedral	11.050 <sup>f</sup>	9.89	11.82	10.93	9.86		1.62	1.58	1.07	1.50
octahedral	11.680 <sup>f</sup>	9.97	12.49	11.68	9.94		1.50	1.50	1.07	1.36

**Table 2.** Energy and relaxation volume of vacancy cluster configurations (see also figure 2). The formation energy of the monovacancy is given, then subsequently the binding energies for the  $a$ th cluster containing  $N$  vacancies defined as  $E_b(N, a) = NE^f(1) - E^f(N, a)$ . Energies are given in eV, relaxation volume in fraction of atomic volume. DFT results from [44]. Other empirical potential results are given in the text. The order parameter  $\chi$  is defined in equation (3). Self-consistent experimental estimates for the monovacancy formation energy are  $3.61 \pm 0.07$  [45] to  $3.77 \pm 0.07$  [46].

Vacancy cluster	Degeneracy	Cluster param $\chi$	Energy		Relax vol	
			DFT	EAM	DFT	EAM
1v1	1		3.619	3.727	−0.37	−0.36
2v1	4	1.00000	0.048	0.170	−0.72	−0.86
2v2	3	1.33333	−0.286	−0.130	−0.79	−1.00
2v3	6	2.66667	−0.063	−0.337	−0.76	−0.85
2v4	12	3.66667	0.042	−0.061		−0.82
2v5	4	4.00000	−0.094	−0.141		−0.77
3v1	12	1.11111	0.311	0.433	−1.08	−1.31
3v2	12	1.55556	0.074	0.058		−1.29
3v3	12	1.77778	−0.257	−0.468		−1.47
3v4	4	2.00000	0.153	0.386		−1.34
3v5	24	2.00000	−0.047	0.006		−1.50
3v6	3	2.66667	−0.348	−0.177		−1.76
4v1	6	1.11111	1.156	1.446		−1.63
4v2	6	1.33333	0.900	1.059		−1.54
4v3	24	1.38889	0.590	0.674		−1.65
4v4	24	2.00000	0.595	0.310		−1.70
5v1	12	1.26667	2.108	2.494		−1.91
5v2	48	1.53333	1.318	1.694		−1.98
6v1	3	1.33333	3.340	3.945		−2.32
6v2	24	1.48889	3.072	3.541		−2.18
7v1	24	1.58730	4.305	4.996		−2.59
8v1	6	1.71429	5.523	6.463		−3.04
8v2	4	1.71429	5.992	6.422		−2.48
9v1	24	1.85185	7.237	7.883		−2.89
10v1	48	2.03704	7.657	9.356		−3.32
10v2	48	2.09630	8.194	8.953		−3.17
11v1	48	2.19394		10.784		−3.63
12v1	48	2.26263		12.652		−3.77
13v1	24	2.43590		14.143		−4.25
14v1	48	2.88645		15.578		−4.60
15v1	1	2.28571		20.025		−3.77

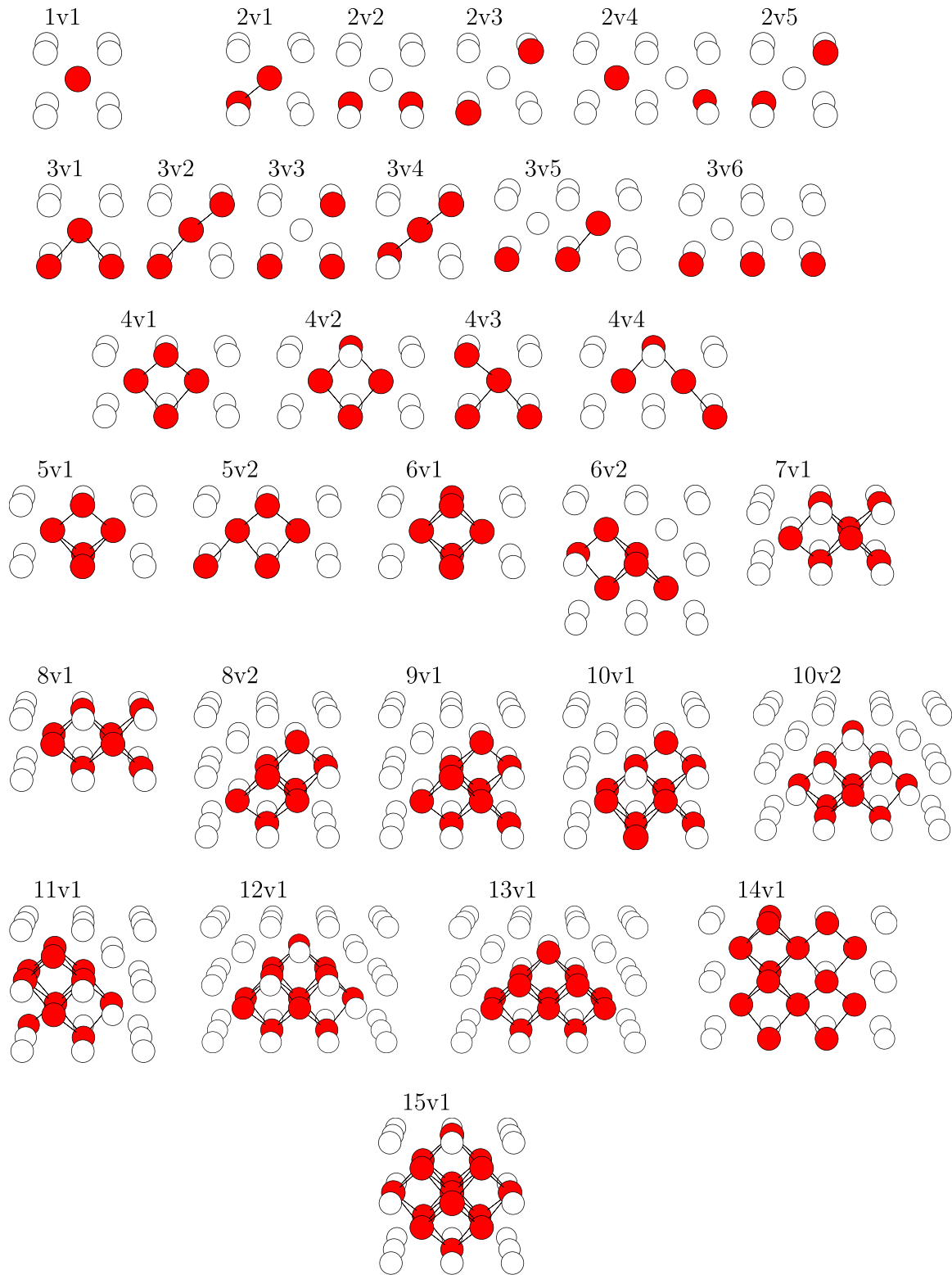


**Figure 2.** The 31 vacancy cluster configurations considered here.

### 3.3. Transition energies

In this section we turn our attention to transition energy barriers between vacancy cluster configurations, computed using the nudged elastic band method [51]. We present here extensive results computed using DFT, which we believe significantly extend the available database of values. A cluster of

$n > 1$  vacancies has several possible bound configurations, some of which we have described in table 2 and figure 2. We can denote a transition for  $n$  vacancies in configuration  $a$  crossing to  $b$  with the code  $nvaxb$ .

Computed transition energies are given in table 3. To generate a statistically comparable result between EAM potentials we considered a larger set of 33 transitions for 1–4



**Table 3.** Vacancy cluster transition energies. The transition  $nvaxb$  takes an  $n$ -vacancy cluster from configuration  $a$  to configuration  $b$  (see figure 2). Other empirical potential results have been computed from analytic forms in (a) Marinica *et al* [23], (b) Derlet *et al* [11], (c) Ackland–Thetford [34]. The simple K–W model for the saddle point energy between configurations  $a$  and  $b$ , as computed with the potential described here, is  $E_s = (E_a + E_b)/2 + 1.75$  eV. In order to better show the differences in the migration energy, the value for the monovacancy migration energy is given in eV, then subsequent columns show the difference, ie the total DFT 2v1x2 migration barrier is  $E_m = E_s - E_a = 1.756 + 0.069 = 1.825$  eV, and for the K–W model  $1.750 + 0.150 = 1.900$  eV. The reverse event (2v2x1) has a K–W migration barrier  $1.750 - 0.150 = 1.600$  eV. A generally accepted experimental range for the 1v1x1' monovacancy migration energy is  $1.68 \pm 0.06$  eV at 1550 K rising to  $2.02 \pm 0.05$  eV at 2600 K [54]. Experiments suggest divacancy migration energies should be similar to that of the monovacancy [48, 55]. To compare different empirical approximations for the transition energies, we compute the error in the sample.

	DFT	This work	Other EAM			Kang–Wienberg [53]
			(a)	(b)	(c)	
1v1x1'	1.756	1.523	2.056	1.845	1.449	1.750
2v1x2	0.069	0.113	0.362	0.191	0.017	0.150
2v1x3	0.051	0.366	0.289	0.482	0.316	0.253
2v1x5	−0.039	−0.054	0.010	0.097	0.045	0.155
3v1x1' <sup>a</sup>	−0.610	0.079	0.492	0.314	−0.023	0
3v1x2	−0.115	0.279	0.332	0.626	0.376	0.188
3v1x3	0.337	0.456	0.543	0.617	0.353	0.451
3v1x5	0.133	0.064	0.340	0.200	0.030	0.213
4v1x3	0.105	0.525	0.645	0.808	0.476	0.386
Error		$-0.21 \pm 0.05$	$0.48 \pm 0.07$	$0.30 \pm 0.07$	$-0.24 \pm 0.05$	$0.04 \pm 0.03$

<sup>a</sup> The trivacancy migration energy is anomalously low (see text), and it may not be possible to reproduce without introducing angular bonding terms. The trivacancy migration energy is therefore excluded from the error calculation.

vacancy clusters, namely forward and backward transitions 1v1x1', 2v1x2, 2v1x3, 2v1x5, 2v2x4, 2v3x4, 2v5x4, 3v1x1', 3v1x2, 3v1x3, 3v1x5, 3v2x3, 3v2x5, 3v4x5, 3v5x5', 3v5x6, 4v1x2, 4v1x3. The results are also presented as a scatter plot in figure 3, including more transitions for clusters up to size 9. We find that the EAM potentials perform similarly well. Our potential gives similar results to AT, slightly underestimating the barriers, whereas CEA-4 and DND slightly overestimate the barriers.

The benchmark figure for comparing vacancy cluster transitions must be the monovacancy migration energy, but it is clear that performing well in this metric alone is insufficient for deciding a good potential for vacancy dynamics. One transition merits special attention. The trivacancy may rapidly diffuse without dissociation purely through nearest-neighbour atom-vacancy exchanges [52]. The DFT nudged-elastic-band calculation finds the saddle point to be a very high symmetry configuration, with four vacant sites tetrahedrally distributed around the migrating atom. This unusual bonding configuration allows for a very low energy migration path. Our DFT calculations predict a trivacancy migration energy of 1.146 eV, which is much lower than the migration energy for the monovacancy (see table 3). The empirical potentials do not find this high-symmetry, low-energy saddle, and so greatly overestimate the tri-vacancy migration energy. An examination of the bond lengths and electron density for the participating atoms suggests that the energy of this special saddle point can not be easily reproduced by modifying the EAM form- it is an example of a situation where angular dependent bonding terms are necessary.

It is also worth noting that the Kang–Weinberg (K–W) model [53],  $E_s \approx (E_a + E_b)/2 + \Delta E$ , yields good saddle points. The magnitude of the barrier  $\Delta E$  can easily be tweaked to exactly reproduce the average saddle point barrier; more importantly we see that the spread of the errors

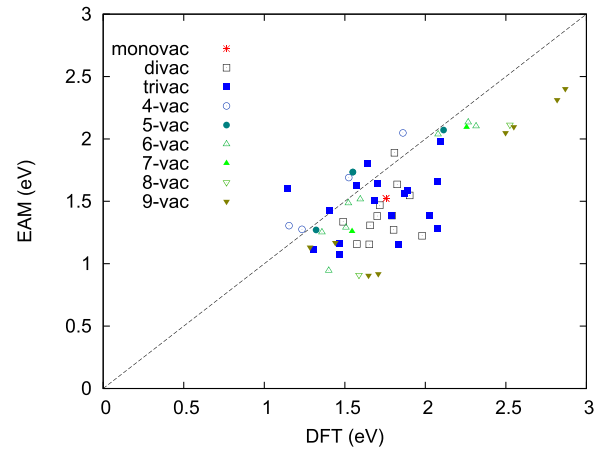


**Figure 3.** Transition energies comparing the EAM potential described here with the DFT computed values using the method described in the text. Other EAM potentials give similar scatter plots; a statistical comparison is given in the text.

(defined as the difference between DFT and empirical result) introduced by this estimate is smaller than that for the EAM potentials. This implies that this very simple saddle point model is a *better* estimate than that of the EAM potentials we have tested.

### 3.4. Surface properties

The surface energy, and interlayer relaxations are important quantities for any simulations which include explicit crystal surfaces, or where voids are of sufficient size that they start to resemble free surfaces locally. Empirical potentials for tungsten have struggled to reproduce these fundamental quantities, adding a layer of uncertainty to results from thin-foil simulations (see table 4). The (110) surface has the lowest energy for many bcc metals, including tungsten. Experimentally the

**Table 4.** Unreconstructed surface properties. Energies in  $\text{eV } \text{\AA}^{-2}$ . Layer relaxation in % ( $\delta_{ij} = 100\% \times \left( \frac{(\bar{z}_i - \bar{z}_j)}{(z_i^0 - z_j^0)} - 1 \right)$ ), where  $\bar{z}_i$  is the average position of an atom in the  $i$ th layer, and  $z_i^0$  the perfect lattice position. DFT values from [57]. Other empirical potential results computed from analytic forms in (a) Marinica *et al* [23], (b) Derlet *et al* [11], (c) Ackland–Thetford [34]. The experimental estimate for the surface energy is  $0.229 \text{ eV } \text{\AA}^{-2}$  [56].

Surface	Energy					Layer relaxation					
	DFT	This work	Other EAM			DFT	This work	Other EAM			
			(a)	(b)	(c)			(a)	(b)	(c)	
(1 1 0)	0.250	0.218	0.156	0.150	0.161	$\delta_{12}$	-3.6	-3.05	-1.13	-0.96	-2.36
						$\delta_{23}$	0.2	0.07	0.02	0.02	0.26
						$\delta_{34}$		0.00	0.00	0.00	0.20
(1 0 0)	0.290	0.239	0.183		0.182	$\delta_{12}$	-6	-2.76	-0.63		-1.19
						$\delta_{23}$	0.5	-0.56	-0.61		-2.96
						$\delta_{34}$		0.23	0.22		1.42
(1 1 1)	0.278	0.257	0.200	0.193	0.206	$\delta_{12}$		-4.48	-4.89	-6.22	-4.40
						$\delta_{23}$		-14.87	-7.48	-10.22	-12.72
						$\delta_{34}$		7.49	4.96	8.34	9.68
(2 1 1)	0.261	0.241	0.186		0.190	$\delta_{12}$		-7.92	-4.85		-5.80
						$\delta_{23}$		0.21	1.06		0.95
						$\delta_{34}$		-2.57	-0.89		-1.03

(1 1 0) surface energy has been determined to be  $0.23 \text{ eV } \text{\AA}^{-2}$  [56] which coincides well with its DFT-computed value  $0.250 \text{ eV } \text{\AA}^{-2}$  [57]. Empirical potentials give significantly (40% or more) lower values. Although the trend from one surface to the next may be adequately reproduced [23], this gross underestimate means additional surface in the form of voids, or surface roughness is far too readily formed. The EAM-type potentials CEA-4, DND and AT give similar results: 0.156, 0.150 and  $0.161 \text{ eV } \text{\AA}^{-2}$  respectively. The bond-order potentials of Mrovec *et al* [58], and Ahlgren *et al* [49] are no better, giving 0.167 and  $0.135 \text{ eV } \text{\AA}^{-2}$  respectively. Juslin *et al* [59] report  $0.09 \text{ eV } \text{\AA}^{-2}$  for the (1 0 0) surface, which should be higher energy. Our explicit modification of the low-electron-density binding has an excellent surface energy,  $0.218 \text{ eV } \text{\AA}^{-2}$ . Results are summarised in table 4.

For the (1 0 0) surface, our EAM potential produces only the  $p(1 \times 1)$  periodicity structure, observed in pure tungsten above room temperature [60], and does not generate the  $(\sqrt{2} \times \sqrt{2})R45^\circ$  unit cell with  $p2mg$  symmetry seen at low temperature and using DFT [60, 61]. In the (1 1 1) orientation, the surface appears as a hexagonal cell with  $(a = \sqrt{2}a_0, c = \sqrt{\frac{3}{4}}a_0)$  and atoms at  $(0, 0, 0), (\frac{1}{3}, \frac{1}{3}, \frac{1}{3}), (\frac{2}{3}, \frac{2}{3}, \frac{2}{3})$ . A slightly lower energy surface (by  $2 \text{ meV } \text{\AA}^{-2}$ ) was found with the EAM potential if the top layer was only half filled, ie a  $c(1 \times 2)$  reconstruction with atoms at  $(0, 0, 0)$  and  $(1, 0, 0)$  removed. The (1 1 0) and (2 1 1) surfaces did not show any reconstructions with the EAM potential.

### 3.5. Vacancy formation energies and transitions at surfaces

Using the EAM potential we have investigated the formation energy of vacancies near the surfaces, and computed the transition energies for vacancy movement to and from the surface.

The supercells used for the calculations were of cuboidal shape, containing about 2000 atoms, and allowed to relax in the direction normal to the surface only. Transitions were computed using the drag method [51], with care taken to identify any metastable states and to ensure smooth paths between replicas. The results are summarised in figure 4.

The following features can be noted as common to all surfaces: The formation energy is low for a vacancy in the surface layers, but rapidly reaches the bulk level by two lattice parameters depth. The vacancy migration energy is also at its bulk level beyond this depth. Strings of atoms can be readily displaced along  $[1 1 1]$  directions, which can destabilise a vacancy immediately below the surface.

A few metastable reconstructions were identified for vacancies immediately below the surface (see figure 4 insets).

## 4. Dissociation of vacancy clusters

We have investigated the dissociation of existing vacancy clusters using the EAM potential and lattice-based atomistic kinetic Monte Carlo. In section 3.3, we concluded that it was better to use a Kang–Wienberg model barrier between two competing vacancy clusters (the average energy of the competing states plus a constant), rather than to compute the barrier using the nudged elastic band method [51] or similar.

We find that whether transitions are considered between elastically relaxed states, or atoms on a rigid lattice, makes a negligible impact on dissociation times. We attribute this to there being no deep elastic minima in the potential energy landscape— a different conclusion would surely be reached if a second phase [62] or interstitial clusters [63] were present. To ensure this methodology is consistent with the migration pathways found in section 3.5, we searched for metastable off-lattice rearrangements for single vacancies near the surface of the 15 vacancy cluster, but found none.



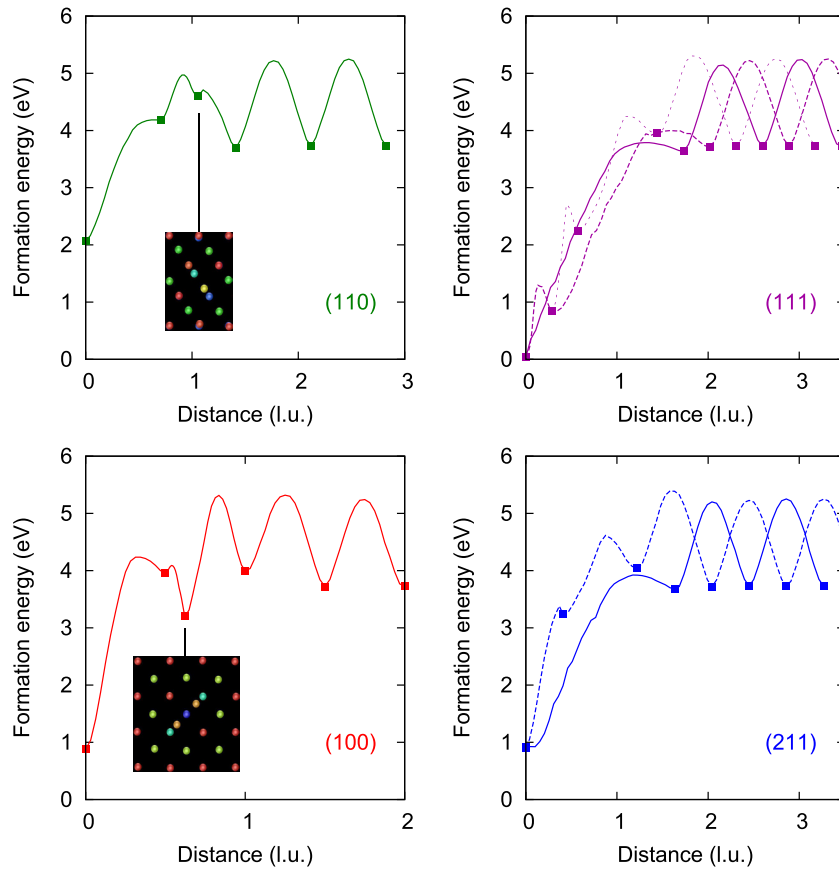


**Figure 4.** Formation energy and transition paths for a single vacancy brought close to a surface using the EAM potential. Insets show reconstructions with atoms colour-coded by depth, (red = layer 1, green = layer 2, blue = layer 3). Notice that close to the (110) and (100) surfaces, the vacancy becomes an extended defect rather than a clearly identifiable single missing atom. We only considered vacancy-atom exchanges parallel to the surface normal. As the (111) direction has three layer repeats, we plot the solid, dashed and dotted lines indicating the energy during vacancy-atom exchanges between sites on a single sublattice, ending either in the first, second or third layers. We did not consider exchanges between sublattices. Similarly the (211) direction has two layer repeats, the solid and dashed line indicate the energy during vacancy-atom exchanges ending in the first and second layers.

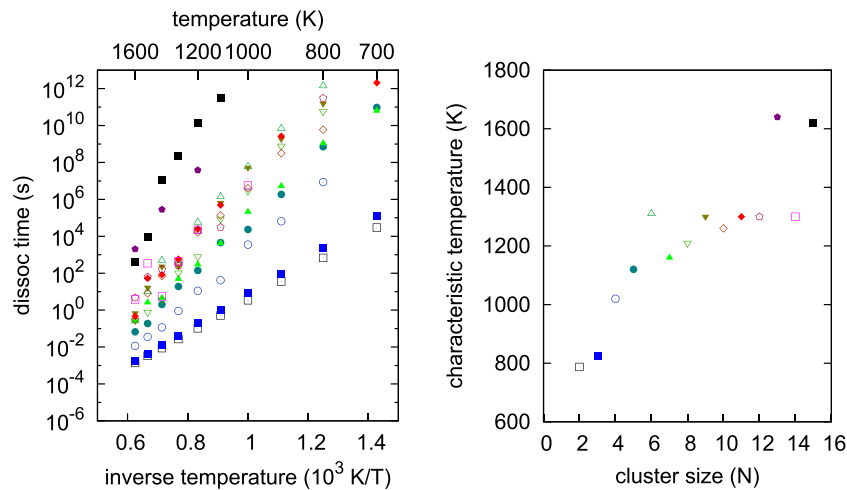


**Figure 5.** (Left) Average vacancy cluster dissociation time and (right) characteristic temperature for dissociation determined by an Arrhenius fit to the data in the left hand panel, as computed by atomistic Kinetic Monte Carlo simulation as described in the text. The symbols on the left-hand plot correspond to the sizes indicated in the right-hand plot.

We used the standard  $n$ -fold way kinetic Monte Carlo algorithm [64] considering all vacancy-atom exchanges each time step, with a K–W model rate for exchange:

$$r_{axb} = \nu_D \exp \left( -\frac{(E_b - E_a)/2 + \Delta E}{k_B T} \right), \quad (4)$$

where  $\nu_D = 6.45 \times 10^{12}$  Hz [20] is close to the Debye frequency and  $\Delta E = 1.75$  eV. The initial configuration was  $13 \times 14 \times 15$  unit cells, with the lowest energy vacancy cluster (as determined in section 3.2) placed in the centre, and dissociation was deemed to have occurred when one or more vacancies separated from the central cluster for 100 steps. The dissociation time was computed at a range of temperatures, and from this a single characteristic temperature for dissociation after one second was found by Arrhenius fitting. The results are shown in figure 5.

We see that small vacancy clusters ( $n < 15$ ) become mobile on an experimental timeframe at a temperature of 1300 K. This can be compared to the point (1373–1673 K) where Ferroni *et al* [27], observed significant loop loss in *in situ* annealing of irradiated tungsten. Our results therefore indicate that one contribution to stage IV resistivity recovery is the dissolution of small vacancy clusters, which consequently allows for detrapping of dislocation loops.

## 5. Conclusions

We have demonstrated a failure of existing empirical potentials to reproduce the vacancy-cluster and surface energy properties of tungsten in low-electron-density regions, and have remedied this by stiffening the embedding function. Our potential reproduces experimental properties of monovacancies in tungsten, with a formation energy 3.73 eV lying in the experimental range  $3.61 \pm 0.07$  [45] to  $3.77 \pm 0.07$  [46]. The monovacancy migration barrier (1.52 eV) is low compared to the established DFT estimate 1.76 eV, but is not unreasonable given the lowest temperature experimental estimate is  $1.68 \pm 0.06$  eV [54] taken at 1550 K. We have shown in section 3.3 that vacancy cluster transitions are generally well reproduced by a very simple fixed-barrier model for the saddle point energy, but that the energy of some transitions requires angular dependent bonding energy terms, outside the standard EAM model. We note that the trivacancy has a very low migration energy (1.146 eV compared to monovacancy 1.756 eV), as it may migrate without cluster dissociation through a very high symmetry saddle.

The divacancy binding energy with the potential detailed here is 0.17 eV, which is a good match to the DFT value 0.05 eV. We have shown that this potential reproduces the relative energy of competing vacancy clusters with high fidelity. The binding energy of a low energy  $n$ -vacancy cluster varies as  $n^{2/3}$ , suggesting the surface energy is the dominant factor.

The (110) surface energy for this potential is  $0.218 \text{ eV } \text{\AA}^{-2}$ , which compares well to the experimental value  $0.229 \text{ eV } \text{\AA}^{-2}$  [56]. We have shown that the potential developed here predicts vacancies are metastable two lattice

parameters below the surface (in the sense of having thermal barriers to atomic rearrangement), but if they come closer then that it is possible for strings of atoms to shift along  $\langle 111 \rangle$  directions, just as crowdions move, and occasionally generate complex metastable rearrangements with off-lattice atomic positions. However, as these states have very low barriers for a second rearrangement where the vacant site ends up on the surface and near-perfect lattice below, we do not expect these states have a significant effect on microstructural evolution.

We believe our potential stands alone in the quality of its surface and vacancy properties for pure tungsten.

## Acknowledgments

The authors would like to thank Leo Ma, CCFE and Andrea Sand, University of Helsinki, for helpful discussions. This work has been carried out within the framework of the EUROfusion Consortium and has received funding from the Euratom research and training programme 2014–2018 under grant agreement No 63305, and from the RCUK Energy Programme [grant number EP/P012450/1]. The views and opinions expressed herein do not necessarily reflect those of the European Commission. DNM would like to acknowledge the EUROfusion for the provision of access to a super-computer (Helios) at the Computational Simulation Centre (CSC) in Rokkasho (Japan) and also to the Marconi super-computer (CINECA, Italy). To obtain further information on the data and models underlying this paper please contact PublicationsManager@ccfe.ac.uk.

## Appendix. Parameterization

The full potential is defined by the energy for atom  $i$  (equation (1)).

$$E_i = \frac{1}{2} \sum_{j \in \mathcal{N}_i} V(r_{ij}) + F[\rho_i], \quad (A.1)$$

where  $\mathcal{N}_i$  denotes the atoms within the cutoff range  $d = 4.400224 \text{ \AA}$ . The potential can be considered as a piecewise polynomials, smoothly transforming to non-polynomial forms. We start by writing the polynomial switching function which switches from 1 for  $x \leq a$  to 0 for  $x \geq b$  and is smooth in first and second derivatives.

$$P(x; a, b) = \begin{cases} 1 & x \leq a \\ \left( \frac{b-x}{b-a} \right)^3 \left( 10 - \left( \frac{b-x}{b-a} \right) \left( 15 - 6 \left( \frac{b-x}{b-a} \right) \right) \right) & a \leq x \leq b \\ 0 & x \geq b \end{cases} \quad (A.2)$$

Then we write the pairwise potential part in the region  $r_{m-1} \leq r \leq r_m$  as

$$V(r) = \left( \sum_k v_{k,m} \left( \frac{r - r_{m-1}}{r_m - r_{m-1}} \right)^k + V_{AT}(r) \right) (1 - P(r; r_{z0}, r_{z1})) + V_{ZBL}(r) P(r; r_{z0}, r_{z1}), \quad (A.3)$$

the electron density as

**Table A1.** Polynomial coefficients, non-polynomial parameters, and piecewise ranges for their applicability. Note that  $V(r > d) = 0$ . All units  $eV \text{ \AA}$ .

Polynomial coefficients					
Pairwise	$r \leq r_1$	$r_1 \leq r \leq r_2$	$r_2 \leq r \leq r_3$	$r_3 \leq r \leq r_4$	$r_4 \leq r \leq r_5$
$v_{0,m}$	$4.852\,068\,738\,744\,85 \times 10^{+02}$	$3.802\,541\,335\,421\,50 \times 10^{+00}$	$-1.492\,428\,790\,706\,26 \times 10^{+00}$	$-1.015\,190\,247\,002\,60 \times 10^{+00}$	$-5.263\,289\,108\,168\,47 \times 10^{-01}$
$v_{1,m}$	$-1.314\,112\,602\,953\,51 \times 10^{+03}$	$-1.536\,940\,444\,410\,54 \times 10^{+01}$	$2.781\,795\,421\,760\,68 \times 10^{-01}$	$4.348\,242\,641\,050\,10 \times 10^{-01}$	$1.052\,657\,821\,633\,69 \times 10^{+00}$
$v_{2,m}$	$1.327\,991\,990\,816\,69 \times 10^{+03}$	$1.743\,694\,704\,100\,20 \times 10^{+01}$	$5.981\,376\,174\,368\,19 \times 10^{-01}$	$1.626\,699\,829\,528\,24 \times 10^{-01}$	$-5.263\,289\,108\,168\,38 \times 10^{-01}$
$v_{3,m}$	$-5.953\,509\,188\,048\,19 \times 10^{+02}$	$-1.336\,414\,612\,096\,27 \times 10^{+01}$	$-6.919\,861\,940\,423\,37 \times 10^{-01}$	$2.127\,019\,665\,632\,22 \times 10^{-01}$	
$v_{4,m}$	$1.000\,671\,984\,023\,94 \times 10^{+02}$	$9.001\,633\,399\,049\,76 \times 10^{+00}$	$2.929\,075\,609\,708\,89 \times 10^{-01}$	$-8.559\,638\,989\,567\,65 \times 10^{-01}$	
$v_{5,m}$		$-3.000\,000\,001\,164\,15 \times 10^{+00}$		$7.773\,578\,008\,043\,81 \times 10^{-01}$	
$v_{6,m}$				$-2.622\,020\,835\,965\,03 \times 10^{-01}$	
$v_{7,m}$				$0.194\,732\,955\,478\,086 \times 10^{-01}$	
Density $r \leq d$					
$\phi_0$	$0.621\,131\,682$				
$\phi_1$	$-0.282\,318\,21$				
$\phi_2$	$0.032\,079\,982$				
Embedding $\rho \leq \rho_-$					
$f_{0,m}$	$0$	$\rho \geq \rho_-$			
$f_{1,m}$	$-5.409\,612\,162\,598 \times 10^{+01}$	$-2.982\,217\,66 \times 10^{+00}$			
$f_{2,m}$	$3.625\,756\,418\,0600 \times 10^{+02}$	$2.858\,583\,59 \times 10^{+00}$			
$f_{3,m}$	$-7.693\,897\,313\,2256 \times 10^{+02}$				
$\bar{A}$	$10.587\,823\,8607$				
Non-polynomial parameters					
A-T					
$b_0$	$2.741\,143\,61$				
$B$	$89.7$				
$\alpha$	$2.0$				
ZBL					
$Z$	$74$				
$a_s$	$0.078\,908$				
$r_{z0}^*$	$1.0$				
$r_{z1}^*$	$1.5$				
Piecewise ranges					
$r_0$	$0.0$				
$r_1$	$2.0$				
$r_2$	$2.7$				
$r_3$	$3.1652$				
$r_4$	$3.52$				
$r_5 = d$	$4.400\,224$				
$\rho_-$	$0.157\,083\,65$				
$\rho_1$	$0.737\,839\,58$				
$\rho_2$	$0.994\,479\,43$				

$$\rho = \sum_{j \in \mathcal{N}_i} \sum_k \phi_k r_{ij}^k, \quad (\text{A.4})$$

and the embedding function as

$$F[\rho] = \begin{pmatrix} \sum_k f_{k,1} \rho^k \\ \sum_k f_{k,2} \rho^k \end{pmatrix}, \quad (\rho \leq \rho_-) \\ = \begin{pmatrix} \sum_k f_{k,1} \rho^k \\ \sum_k f_{k,2} \rho^k \end{pmatrix} P(\rho; \rho_1, \rho_2) - \tilde{A}(\sqrt{\rho} - \rho) (1 - P(\rho; \rho_1, \rho_2)), \quad (\rho \geq \rho_-) \quad (\text{A.5})$$

$V_{\text{AT}}(r)$  in the pairwise potential is the Ackland–Thetford correction [34],

$$V_{\text{AT}}(r) = \Theta(b_0 - r) B(b_0 - r)^3 \exp(-\alpha r) \quad (\text{A.6})$$

and  $V_{\text{ZBL}}(r)$  the ZBL universal screening potential, given by [36]

$$V_{\text{ZBL}}(r) = \frac{Z^2}{4\pi\epsilon_0 r} \left[ \frac{0.1818 \exp(-3.2r/a_s) + 0.5099 \exp(-0.9423r/a_s)}{+0.2802 \exp(-0.4029r/a_s) + 0.02817 \exp(-0.2016r/a_s)} \right]. \quad (\text{A.7})$$

The polynomial coefficients (together with their piecewise ranges) and the other parameters are given in table A1. We have cast the parameterization in a gauge where  $\rho = 1$  is the equilibrium level and  $F[0] = F[1] = 0$ . This choice facilitates the construction of alloy or multicomponent potentials [65].

## ORCID iDs

D R Mason  <https://orcid.org/0000-0002-1536-6254>

## References

- [1] Gilbert M and Sublet J-C 2011 Neutron-induced transmutation effects in W and W-alloys in a fusion environment *Nucl. Fusion* **51** 043005
- [2] Gilbert M, Dudarev S, Zheng S, Packer L and Sublet J-C 2012 An integrated model for materials in a fusion power plant: transmutation, gas production, and helium embrittlement under neutron irradiation *Nucl. Fusion* **52** 083019
- [3] Rieth M et al 2011 Review on the EFDA programme on tungsten materials technology and science (*Proc. of ICFRM-14*) *J. Nucl. Mater.* **417** 463–7
- [4] Rieth M et al 2013 Recent progress in research on tungsten materials for nuclear fusion applications in europe *J. Nucl. Mater.* **432** 482–500
- [5] Bolt H, Barabash V, Federici G, Linke J, Loarte A, Roth J and Sato K 2002 Plasma facing and high heat flux materials—needs for ITER and beyond *J. Nucl. Mater.* **307–11** 43–52
- [6] Armstrong D, Hardie C, Gibson J, Bushby A, Edmondson P and Roberts S 2015 Small-scale characterisation of irradiated nuclear materials: part II nanoindentation and micro-cantilever testing of ion irradiated nuclear materials *J. Nucl. Mater.* **462** 374–81
- [7] Tanno T, Fukuda M, Nogami S and Hasegawa A 2011 Microstructure development in neutron irradiated tungsten alloys *Mater. Trans.* **52** 1447–51
- [8] Hofmann F, Mason D, Eliason J, Maznev A, Nelson K and Dudarev S 2015 Non-contact measurement of thermal diffusivity in ion-implanted nuclear materials *Sci. Rep.* **15** 16042
- [9] Dudarev S 2013 Density functional theory models for radiation damage *Annu. Rev. Mater. Res.* **43** 35–61
- [10] Gilbert M R, Dudarev S L, Derlet P M and Pettifor D G 2008 Structure and metastability of mesoscopic vacancy and interstitial loop defects in iron and tungsten *J. Phys.: Condens. Matter* **20** 345214
- [11] Derlet P M, Nguyen-Manh D and Dudarev S L 2007 Multiscale modeling of crowdion and vacancy defects in body-centered-cubic transition metals *Phys. Rev. B* **76** 054107
- [12] Björkas C, Nordlund K and Dudarev S L 2009 Modelling radiation effects using the *ab initio* based tungsten and vanadium potentials *Nucl. Instrum. Methods B* **267** 3204–8
- [13] Sand A E, Dudarev S L and Nordlund K 2013 High-energy collision cascades in tungsten: dislocation loops structure and clustering scaling laws *Europhys. Lett.* **103** 46003
- [14] Yi X, Sand A E, Mason D R, Kirk M A, Roberts S G, Nordlund K and Dudarev S L 2015 Direct observation of size scaling and elastic interaction between nano-scale defects in collision cascades *Europhys. Lett.* **110** 36001
- [15] Setyawan W, Nandipati G, Roche K J, Heinisch H L, Wirth B D and Kurtz R J 2015 Displacement cascades and defects annealing in tungsten, part I: defect database from molecular dynamics simulations *J. Nucl. Mater.* **462** 329–37
- [16] Juslin N and Wirth B 2013 Interatomic potentials for simulation of He bubble formation in W *J. Nucl. Mater.* **432** 61–66
- [17] Jäger W and Wilkens M 1975 Formation of vacancy-type dislocation loops in tungsten bombarded by 60 keV Au ions *Phys. Status Solidi a* **32** 89–100
- [18] Yi X, Jenkins M, Briceño M, Roberts S, Zhou Z and Kirk M 2013 *In situ* study of self-ion irradiation damage in W and W-5Re at 500 C *Phil. Mag.* **93** 1715–38
- [19] Mason D, Yi X, Kirk M and Dudarev S 2014 Elastic trapping of dislocation loops in cascades in ion-irradiated tungsten foils *J. Phys.: Condens. Matter* **26** 375701
- [20] Becquart C, Domain C, Sarkar U, Backer A D and Hou M 2010 Microstructural evolution of irradiated tungsten: *ab initio* parameterisation of an OKMC model *J. Nucl. Mater.* **403** 75–88
- [21] Muzyk M, Nguyen-Manh D, Kurzydowski K J, Baluc N L and Dudarev S L 2011 Phase stability, point defects, and elastic properties of W-V and W-Ta alloys *Phys. Rev. B* **84** 104115
- [22] Becquart C and Domain C 2007 *Ab initio* calculations about intrinsic point defects and He in W *Nucl. Instrum. Methods Phys. Res. B* **255** 23–26 (Computer simulation of radiation effects in solids)
- [23] Marinica M-C, Ventelon L, Gilbert M R, Provile L, Dudarev S L, Marian J, Bencteux G and Willaime F 2013 Interatomic potentials for modelling radiation defects and dislocations in tungsten *J. Phys.: Condens. Matter* **25** 395502
- [24] Bonny G, Terentyev D, Bakaev A, Grigorev P and Neck D V 2014 Many-body central force potentials for tungsten *Modell Simul. Mater. Sci. Eng.* **22** 053001
- [25] Lu G-H, Zhou H-B and Becquart C S 2014 A review of modelling and simulation of hydrogen behaviour in tungsten at different scales *Nucl. Fusion* **54** 086001
- [26] Sand A, Dequeker J, Becquart C, Domain C and Nordlund K 2016 Non-equilibrium properties of interatomic potentials in cascade simulations in tungsten *J. Nucl. Mater.* **470** 119–27
- [27] Ferroni F, Yi X, Arakawa K, Fitzgerald S P, Edmondson P D and Roberts S G 2015 High temperature annealing of ion irradiated tungsten *Acta Mater.* **90** 380–93
- [28] Wróbel J S, Nguyen-Manh D, Kurzydowski K J and Dudarev S L 2017 A first-principles model for anomalous segregation in dilute ternary tungsten-rhenium-vacancy alloys *J. Phys.: Condens. Matter* **29** 145403

- [29] Kato D, Iwakiri H and Morishita K 2011 Formation of vacancy clusters in tungsten crystals under hydrogen-rich condition *J. Nucl. Mater.* **417** 1115–8 (*Proc. of ICFRM-14*)
- [30] Fernandez N, Ferro Y and Kato D 2015 Hydrogen diffusion and vacancies formation in tungsten: density functional theory calculations and statistical models *Acta Mater.* **94** 307–18
- [31] Becquart C and Domain C 2009 A density functional theory assessment of the clustering behaviour of He and H in tungsten *J. Nucl. Mater.* **386–388** 109–11
- [32] Perez D, Sandoval L, Blondel S, Wirth B, Uberuaga B and Voter A 2017 The mobility of small vacancy/helium complexes in tungsten and its impact on retention in fusion-relevant conditions *Sci. Rep.* **7** 2522
- [33] Finnis M W and Sinclair J E 1984 A simple empirical n-body potential for transition metals *Phil. Mag. A* **50** 45–55
- [34] Ackland G and Thetford R 1987 An improved n-body semi-empirical model for body-centred cubic transition metals *Phil. Mag. A* **56** 15–30
- [35] Fikar J and Schäublin R 2009 Molecular dynamics simulation of radiation damage in bcc tungsten (*Fusion Reactor Materials Proc. of the 13th Int. Conf. on Fusion Reactor Materials*) *J. Nucl. Mater.* **386–8** 97–101
- [36] Ziegler J, Biersack J and Littmark U 1982 *The Stopping and Range of Ions in Solids* (Oxford: Pergamon)
- [37] Olsson P, Becquart C S and Domain C 2016 *Ab initio* threshold displacement energies in iron *Mater. Res. Lett.* **4** 219–25
- [38] Kresse G and Hafner J 1993 *Ab initio* molecular dynamics for liquid metals *Phys. Rev. B* **47** 558–61
- [39] Kresse G and Furthmüller J 1996 Efficient iterative schemes for *ab initio* total-energy calculations using a plane-wave basis set *Phys. Rev. B* **54** 11169–86
- [40] Kresse G and Furthm J 1996 Efficiency of *ab initio* total energy calculations for metals and semiconductors using a plane-wave basis set *Comput. Mater. Sci.* **6** 15–50
- [41] Perdew J P, Burke K and Ernzerhof M 1996 Generalized gradient approximation made simple *Phys. Rev. Lett.* **77** 3865–8
- [42] Nguyen-Manh D and Dudarev S 2015 Trapping of He clusters by inert-gas impurities in tungsten: first-principles predictions and experimental validation *Proc. of the 12th Int. Conf. on Computer Simulation of Radiation Effects in Solids (Alacant, Spain, 8–13 June 2014)* *Nucl. Instrum. Methods Phys. Res. B* **352** 86–91
- [43] Nguyen-Manh D, Horsfield A P and Dudarev S L 2006 Self-interstitial atom defects in bcc transition metals: group-specific trends *Phys. Rev. B* **73** 020101
- [44] Hofmann F, Nguyen-Manh D, Gilbert M, Beck C, Eliason J, Maznev A, Liu W, Armstrong D, Nelson K and Dudarev S 2015 Lattice swelling and modulus change in a helium-implanted tungsten alloy: x-ray micro-diffraction, surface acoustic wave measurements, and multiscale modelling *Acta Mater.* **89** 352–63
- [45] Mundy J N 1982 Electrical resistivity-temperature scale of tungsten *Phil. Mag. A* **46** 345–9
- [46] Ehrhart P, Jung P, Schultz H and Ullmaier H 1991 *Atomic Defects in Metals* vol 25 (Berlin: Springer)
- [47] Ventelon L, Willaime F, Fu C-C, Heran M and Ginoux I 2012 *Ab initio* investigation of radiation defects in tungsten: structure of self-interstitials and specificity of di-vacancies compared to other bcc transition metals (Microstructure properties of irradiated materials); *J. Nucl. Mater.* **425** 16–21
- [48] Park J Y, Huang H C W, Siegel R W and Balluffi R W 1983 A quantitative study of vacancy defects in quenched tungsten by combined field-ion microscopy and electrical resistometry *Phil. Mag. A* **48** 397–419
- [49] Ahlgren T, Heinola K, Juslin N and Kuronen A 2010 Bond-order potential for point and extended defect simulations in tungsten *J. Appl. Phys.* **107** 033516
- [50] Bangwei Z, Yifang O, Shuzhi L and Zhanpeng J 1999 An analytic MEAM model for all BCC transition metals *Phys. B: Condens. Matter* **262** 218–25
- [51] Henkelman G, Jóhannesson G and Jónsson H 2002 *Methods for Finding Saddle Points and Minimum Energy Paths* (Netherlands: Springer) pp 269–302
- [52] Barouh C, Schuler T, Fu C-C and Jourdan T 2015 Predicting vacancy-mediated diffusion of interstitial solutes in  $\alpha$ -Fe *Phys. Rev. B* **92** 104102
- [53] Kang H C and Weinberg W H 1989 Dynamic Monte Carlo with a proper energy barrier: surface diffusion and two-dimensional domain ordering *J. Chem. Phys.* **90** 2824–30
- [54] Mundy J, Ockers S and Smedskjaer L 1987 Vacancy migration enthalpy in tungsten at high temperatures *Mater. Sci. Forum* **15–18** 199–204
- [55] Rasch K-D, Siegel R W and Schultz H 1980 Quenching and recovery investigations of vacancies in tungsten *Phil. Mag. A* **41** 91–117
- [56] de Boer F, Boom R, Mattens W, Miedema A and Niessen A 1988 *Cohesion in Metals* (Amsterdam: North-Holland)
- [57] Vitos L, Ruban A, Skriver H and Koll J 1998 The surface energy of metals *Surf. Sci.* **411** 186–202
- [58] Mrovec M, Gröger R, Bailey A G, Nguyen-Manh D, Elsässer C and Vitek V 2007 Bond-order potential for simulations of extended defects in tungsten *Phys. Rev. B* **75** 104119
- [59] Juslin N, Erhart P, Trskelin P, Nord J, Henriksson K O E, Nordlund K, Salonen E and Albe K 2005 Analytical interatomic potential for modeling nonequilibrium processes in the W-C-H system *J. Appl. Phys.* **98** 123520
- [60] Debe M K and King D A 1977 Space-group determination of the low-temperature W001( $\sqrt{2}$ )r45 surface structure by low-energy-electron diffraction *Phys. Rev. Lett.* **39** 708–11
- [61] Heinola K and Ahlgren T 2010 First-principles study of H on the reconstructed W(100) surface *Phys. Rev. B* **81** 073409
- [62] Mason D R, Rudd R E and Sutton A P 2004 Atomistic modelling of diffusional phase transformations with elastic strain *J. Phys.: Condens. Matter* **16** S2679
- [63] Xu H, Osetsky Y N and Stoller R E 2011 Simulating complex atomistic processes: on-the-fly kinetic Monte Carlo scheme with selective active volumes *Phys. Rev. B* **84** 132103
- [64] Bortz A, Kalos M and Lebowitz J 1975 A new algorithm for Monte Carlo simulation of Ising spin systems *J. Comput. Phys.* **17** 10–8
- [65] Bonny G, Grigorev P and Terentyev D 2014 On the binding of nanometric hydrogen-helium clusters in tungsten *J. Phys.: Condens. Matter* **26** 485001